DDRX and CDRX of an as-cast nickel-based superalloy during hot compression at γ′ sub-/super-solvus temperatures

Bingchao Xie [1], Hao Yu [1], Tao Sheng [1], Yuhang Xiong [1], Yongquan Ning [1], M.W. Fu[2]*

[1] School of Materials Science and Engineering, Northwestern Polytechnical University, Xi'an 710072, P.R. China

[2] Department of Mechanical Engineering, the Hong Kong Polytechnic University, Kowloon, Hong Kong, P.R. China

CORRESPONDING AUTHOR:

(*) Dr. Bingchao Xie

E-mail: bcx0314@163.com (Bingchao Xie)

ABSTRACT

Taking the importance of γ′ phase into consideration, an as-cast nickel-based superalloy was investigated by uniaxial compression experiments performed at sub-solvus and super-solvus temperatures. Several different strains were utilized to trace the processes of deformation and microstructural evolution. Electron backscatter diffraction was employed to characterize the microstructures. The results reveal that the volume fraction of DRX grains increased with strain at both sub-solvus and super-solvus temperatures, and also the fraction of high angle grain boundaries. Meanwhile, both the correlated and uncorrelated misorientations gradually approached the random distribution curves during continuous strains. Specially, the fast migration of grain boundaries caused by the unpinning from γ′ particles promoted twin nucleation and generated a number of twins at sub-solvus temperatures. Sub-solvus deformations were found to be more efficient to weaken the initial textures of as-cast superalloys. Finally, it was confirmed that discontinuous dynamic recrystallization (DDRX) dominated the DRX process during the hot deformation carried out at both sub-solvus and super-solvus temperatures. Continuous dynamic recrystallization (CDRX) was the second mechanism, and played a very important role during plastic deformation at sub-solvus temperatures, which is different from the DRX mechanisms reported in the fine-grain structures of wrought billets. The findings improve the understanding of DDRX and CDRX, which does benefit to the accurate control of microstructures of nickel-based superalloys, and also tailoring the properties of final components used in aero-engine.

1 **Keywords:**

2 Nickel-based superalloys; Microstructural evolution; DDRX; CDRX;

3

1. Introduction

During hot deformation, dynamic recovery (DRV) process is slow due to the low stacking fault energy (SFE) of nickel-based superalloys. Therefore, dynamic recrystallization (DRX) is the dominant mechanism that controls the microstructural evolution during deformation [1-3]. DRX is classified into three categories according to phenomenological classification, i.e., geometric dynamic recrystallization (GDRX), discontinuous dynamic recrystallization (DDRX) and continuous dynamic recrystallization (CDRX) [4]. GDRX is considered to take place at high strains (~5–10), where the deformed grains thin to the dimensions of the subgrains diameter [5]. CDRX is characterized by progressive lattice rotation [6]. There is no recognizable 'nucleation' and 'growth' of the DRX grains and the microstructure evolves relatively homogeneously throughout the materials [7]. DDRX has clear nucleation and growth stages. New grains originate at the deformed grain boundaries, but, the dislocation density of new grains increases as continuous strain, thus reducing the driving force for further growth, and the DRX grains eventually cease to grow [1]. Subsequently, new grains may also nucleate at the migrating boundaries, and thus DRX grain bands form along the initial grain boundaries (GBs). DRX mechanisms strongly depend on the processing conditions. For nickel-based superalloys, DRX plays a vital part in the dynamic microstructural evolution during cogging or forging processes, which dramatically affects the properties of final products. Therefore, comprehensive understanding of DRX is a prerequisite for tailoring the mechanical properties of products.

Many investigations have been done to improve the understanding of microstructural evolution and enhance the mechanical properties of nickel-based superalloys [8-15]. Previous researches [3, 16-23] demonstrated that DDRX via grain boundary bulging dominated the

DRX process during the deformation of several nickel-based superalloys, such as Allvac 718Plus, Udimet 720Li, FGH4096, etc. DDRX strongly depended on the pre-existing GBs, which were the potential nucleation sites of DDRX. Some reports showed that the grain boundary area per unit volume affected DRX behaviors dramatically and thus resulted in difficulties of grain refinement in coarse-grain structures of nickel-based superalloys [24-27]. Furthermore, the existence of γ' phase obviously restrained the migration of dislocation, subgrain boundaries and GBs, and finally affected the DRX behaviors [28-30]. However, most of the investigations were based on the as-forged billets with relative fine grains. The ingot structure comprises columnar and equiaxed grains whose diameter is of the order of several millimeters after homogenization treatment and which bear the signature of a marked solidification texture [31, 32]. The grain size strongly affected both the flow behavior and the DRX behavior during the hot deformation process of superalloys. Investigation [33] on three structures with different grain sizes from Udimet 720Li wrought billets revealed that coarse grains and mixed grains have similar flow stress, both greater than the fine grains. Meanwhile, at super-solvus temperature deformation, the fine grains were found easier to nucleate than the other two structures. And the three structures with different grain sizes also expressed very different DRX behaviors at sub-solvus deformation. In addition, there are significant differences in grain boundary distribution, the morphology and volume fraction of γ' phase and the kinetics of DRX between the as-cast and as-forged superalloys [34, 35]. Therefore, the features of as-cast superalloys are necessary to be taken into account during the investigations of deformation and microstructural evolution.

The present work investigated the hot deformation process of an as-cast nickel-based superalloy, i.e., the initial upsetting operation process. Special attentions were focused on the microstructural evolution and its mechanisms associated with DRX. Systematic strains were

utilized to trace the whole deformation processes in the γ single phase region and γ′+γ double phase region. The evolution of GBs, texture and microstructure was discussed based on the data from electron backscatter diffraction (EBSD). And finally, the DRX mechanisms were discussed and the dominant one was confirmed.

2. Material and experiments

The material used in the present work was an ingot measuring a diameter and length of 200 mm and 800 mm, which was manufactured by vacuum-induction melting and vacuum-arc re-melting methods. The chemical composition (wt.%) is: 16.00Cr-13.00Co-1.00Fe-3.70Ti-2.10Al-0.70Nb-4.00Mo-4.00W-0.02C-(Bal.)Ni, and the γ′ solvus temperature was estimated to be about 1119 °C. Fig. 1(a) presents the typical microstructure of the as-received superalloy contained equiaxed grains with a mean equivalent diameter of 631.62 μm, and Fig. 1(b) the secondary and tertiary γ′ precipitates in the casting superalloy. The secondary precipitates initially grow and then split into smaller spherical precipitates during cooling process after casting operation [36] and hence two different morphologies occurred, as shown in Figs. 1(c) and (d). The flower-like precipitates measured a mean equivalent diameter of 1460.48 nm and the spherical precipitates measured a mean equivalent diameter of 477.06 nm. The tertiary γ′ precipitates ranged from 21 to 86 nm (mean equivalent diameter). No additional heat treatment was carried out prior to the hot deformation to reserve the original casting structure.

Cylindrical samples, with a diameter and height of 10 mm and 15 mm, respectively, were machined from the region at the half of radius of the ingot. The longitudinal axes of the samples were parallel with the axis of ingot to simulate the initial upsetting operations prior to the subsequent cogging operations. Uniaxial compression testes were then performed using

the Gleeble-3500 simulator at sub-solvus and super-solvus temperatures (1110 and 1140 °C) and a constant strain rate (0.01 s^{-1}), followed by water quenching (WQ). Several different height reductions (10%, 30% and 50%) were utilized to trace the processes of deformation and microstructural evolution. Tantalum foils with the thickness of 0.1 mm were placed between sample and die to minimize the friction and avoid adhesion. Prior to deformation, the samples were heated up to the working temperature at a heating rate of 10 °C/s and then held for 5 min to ensure temperature equilibrium.

After deformation, all specimens were sectioned parallel to the loading direction through the centerline. The specimens for electron backscatter diffraction (EBSD) scans were mechanically ground and then polished using a Buehler VibroMet 2 polisher. EBSD tests were carried out by a Tescan MIRA3 XM field emission gun scanning electron microscopy (FEGSEM). The data were collected from a rectangular area at the processed sample center using a 425×320 grid and the scanning step size ranged from 0.6 to 6 μm depending on the grain size. The length and width of the rectangle were orthogonal and parallel to the compression direction, respectively. Subsequently, the Oxford Instruments' HKL Channel 5 software was used to analyze the EBSD data, including calculating the average grain size, generating orientation imaging microscopy (OIM) maps, kernel average misorientation (KAM) maps, etc. It should be note that all the microstructure images obtained from EBSD data have been cut into a unitive magnification to provide a visualized comparison about the grain size. But all the statistical information was reserved completely, including grain size, misorientation angle distribution, texture information, etc. In addition, FEGSEM and transmission electron microscope (TEM) were also used to characterize the γ′ precipitates and microstructures in this work.
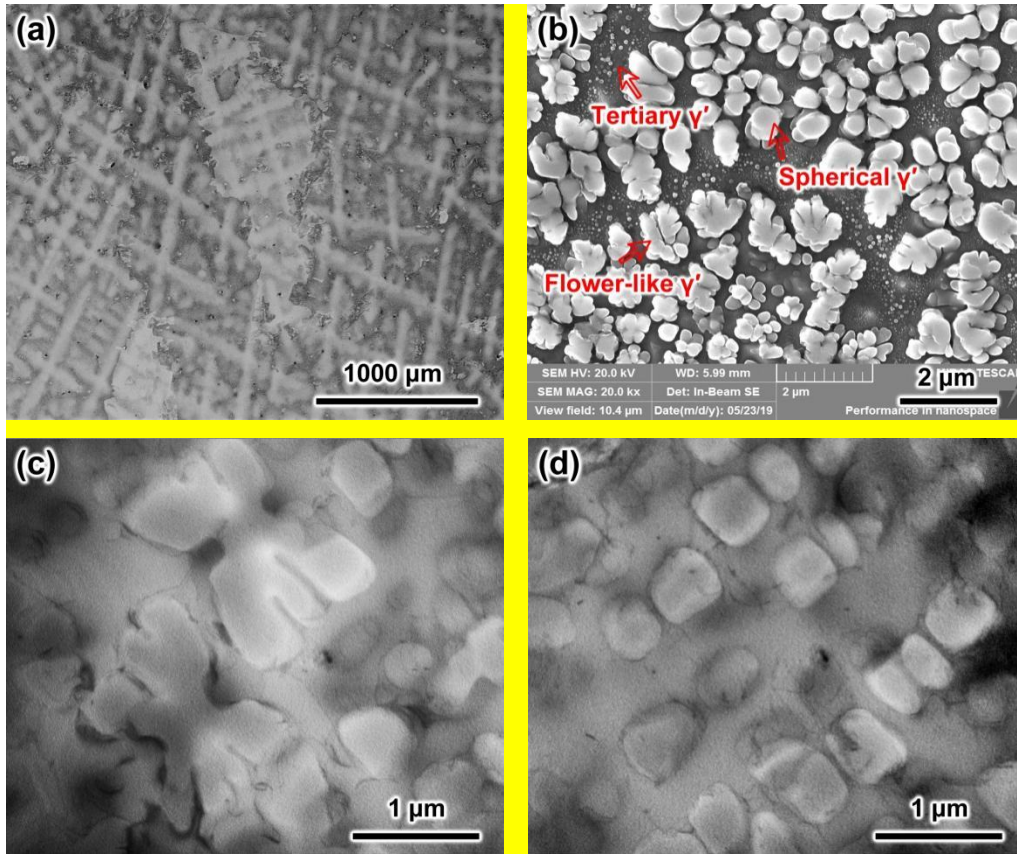
3. Results and discussion

3.1 Evolution of grain structures and boundaries

Fig. 2 presents the stress-strain curve obtained at the deformation temperature of 1110 °C and the strain rate of 0.01 s^{-1}, as well as the EBSD grain boundary maps at different strains. As shown in Fig. 2(a), the flow stress rapidly increased with the increasing strain. At this stage, strain hardening was the dominant factor that determined the flow behaviors, caused by the generation and multiplication of dislocations. When a transient balance

between the dislocation multiplication and annihilation occurred, peak stress was achieved. Subsequently, true stress fell gradually due to DRV and DRX. The strain rate of hot deformation used in this research is 0.01 s^{-1}, and thus the steady state was absent due to the lack of time for achieving balanced materials softening and hardening [37-39]. Meanwhile, the strain hardening rate was also plotted in Fig. 2(a). Corresponding to the sharp increase of stress at the beginning of deformation, the strain-hardening rate fell from 5153 to 0 MPa. The strain-hardening rate fluctuated around -100 MPa after the peak stress, which was consistent with the absence of the steady state. Fig. 2(b), (c) and (d) are the grain boundary maps captured at the strains of 0.11, 0.36 and 0.69, respectively. For the sample compressed to the strain of 0.11 (Fig. 2(b)), few substructure-free grains were observed nearby the initial high angle grain boundaries (HAGBs), and large amount of low angle grain boundaries (LAGBs) formed within the deformed grains. Meanwhile, grain boundary bulging were also observed at this sample, which benefited to DRX nucleation [3]. DRX process was restrained by the deformation stored energy at this stage. Therefore, the original coarse grains and few DRX grains co-existed here. As strain increased to 0.36, DRX grains, with a mean equivalent diameter of 9.62 μm, could be observed clearly in the interior of the deformed grains due to the increasing deformation stored energy (Fig. 2(c)). Increasing strain provided more driving force for the movement of dislocations and migration of boundaries [40]. Hence, the DRX fraction (27.78%) increased with strain significantly. Supported by sufficient deformation stored energy, the DRX nuclei grew gradually by consuming the deformed grains and finally replaced the deformed grains completely, as shown in Fig. 2(d). When the sample was compressed to the strain of 0.69, DRX process almost completed although the microstructure was not uniform. The DRX fraction was 93.41% but the DRX grains just grew slightly (a mean equivalent diameter of 10.13 μm), which substantiated that the Smith-Zener pinning of the γ′ phase strongly restrained the coarsening of DRX grains at sub-solvus temperatures

(1110 °C in this case). In general, most of the new DRX grains first occurred nearby the initial HAGBs and then developed towards the center areas of the deformed grains, and finally replaced the original grains [3, 41]. Meanwhile, it could also be clearly observed that the residual deformed grains were separated by several subgrain boundaries, which would discussed at section 3.3.2 in detail.

Higher temperature provided more driving force for the movement of dislocations and migration of boundaries [42, 43]. It accelerated the DRX process to a certain extent. Therefore, the dynamic softening was more obvious at 1140 °C by comparison with that at 1110 °C. Correspondingly, at the initial deformation stage, the original strain-hardening rate (3162 MPa) is lower than that of the deformation performed at 1110 °C (Fig. 3(a)). As shown in Fig. 3(c) and (d), the DRX grains grew from 13.42 μm to 27.22μm (mean equivalent diameter) when the strain increased from 0.36 to 0.69 at 1140 °C, which were both obviously coarser than that at 1110 °C at corresponding strain. Meanwhile, the DRX fraction also increased from 34% to 100%. It should be note that the DRX grains significantly coarsened with the increase of strain during the deformation at 1140 °C. Two factors resulted into a higher DRX degree and coarser DRX grains when the sample was deformed at a super-solvus temperature. One was that a higher deformation temperature provides a higher grain boundary mobility. The more important one was that the absence of γ′ phase decreased the resistance of the movement of GBs [44], which can be substantiated by Fig. 4. With a close observation in Fig 4, fine γ′ precipitates (mean equivalent diameter of 38 nm) occurred in Fig. 4 (a) and (c) despite the two samples were both quenched by water from a γ′ super-solvus temperature (1140 °C). In addition, finer precipitates (mean equivalent diameter of 30 nm) were also observed in the samples deformed at 1110 °C, which were very different from the tertiary γ′ precipitates in the original as-casting ingot (Fig. 1(b)) and could be due to the

partly dissolving of tertiary γ' precipitates during hot deformation at 1110 °C and subsequent precipitation during water quenching process. Therefore, this kind of γ' precipitates has been considered to form during the water quenching process and should be neglected during the discussion of the hot deformation [45, 46]. Hence, it could be confirmed that γ' precipitates fully dissolved in the samples deformed at 1140 °C, which favored the coarsening of DRX grains. In addition, the microstructure obtained at the temperature of 1140 °C and the strain of 0.69 was also not uniform due to abnormal growth, i.e., an abnormal grain growth (AGG) structure. Similar AGG has been observed in a model nickel-based superalloy [47] and also in pure polycrystalline Ni metal [48]. Boundary segments moving by a boundary step mechanism is responsible for the AGG phenomenon [49, 50].
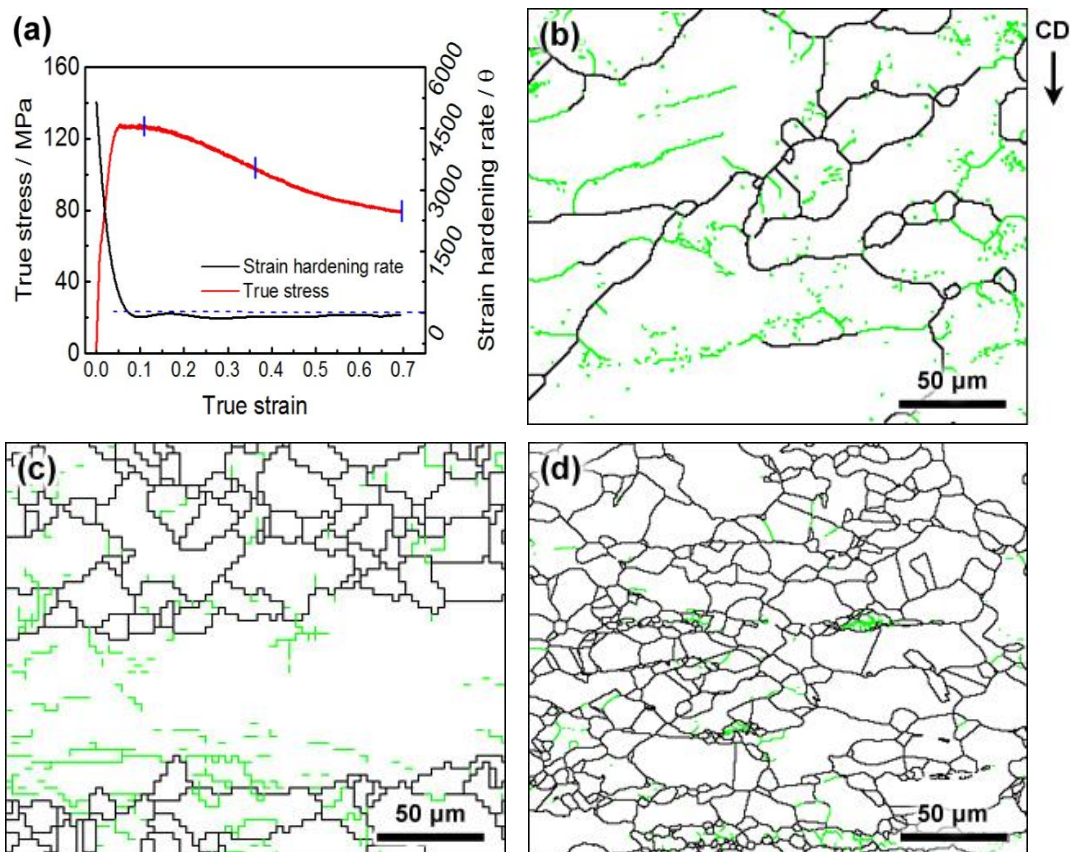
1 **Fig. 2** (a) Stress-strain curve obtained at the temperature of 1110 °C and grain boundary

2 maps at the strains of (b) 0.11, (c) 0.36 and (d) 0.69. The black lines represent HAGBs and

3 the green lines represent LAGBs. CD means the compression direction.

4
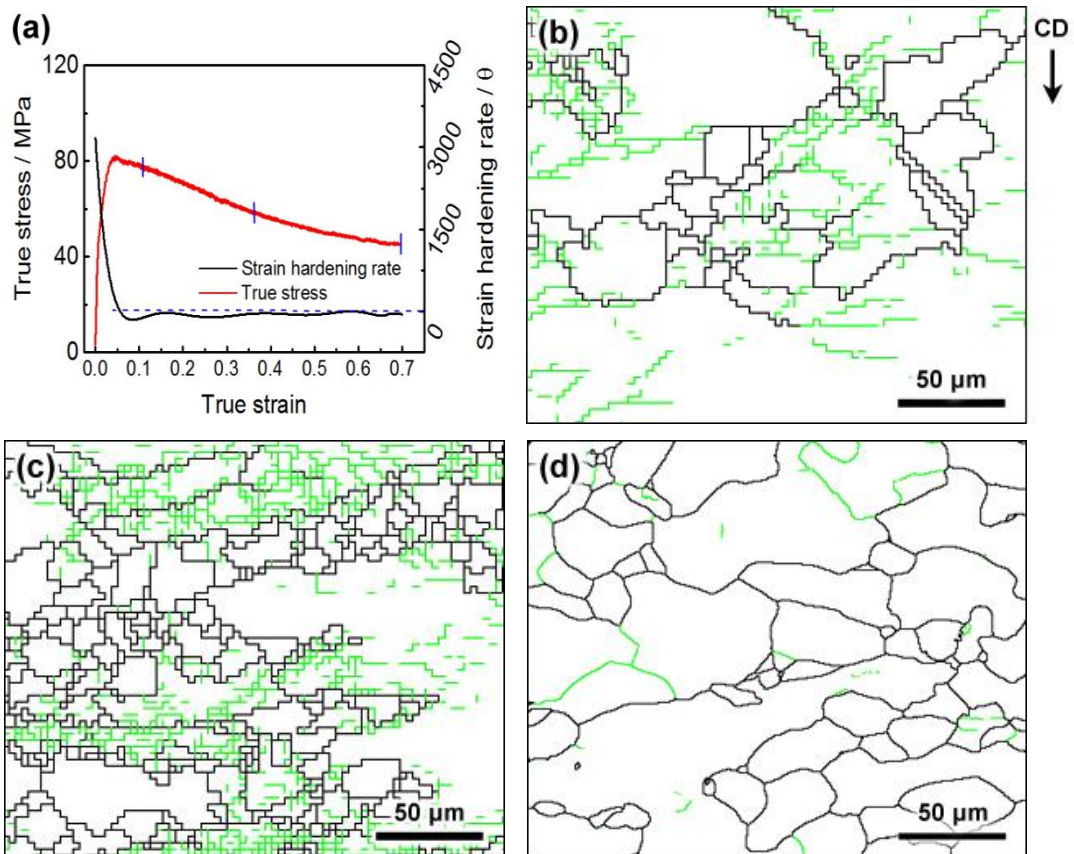
5

6 **Fig. 3** (a) Stress-strain curve obtained at the temperature of 1140 °C and grain boundary

7 maps at the strains of (b) 0.11, (c) 0.36 and (d) 0.69. The black lines represent HAGBs and

8 the green lines represent LAGBs. CD means the compression direction.
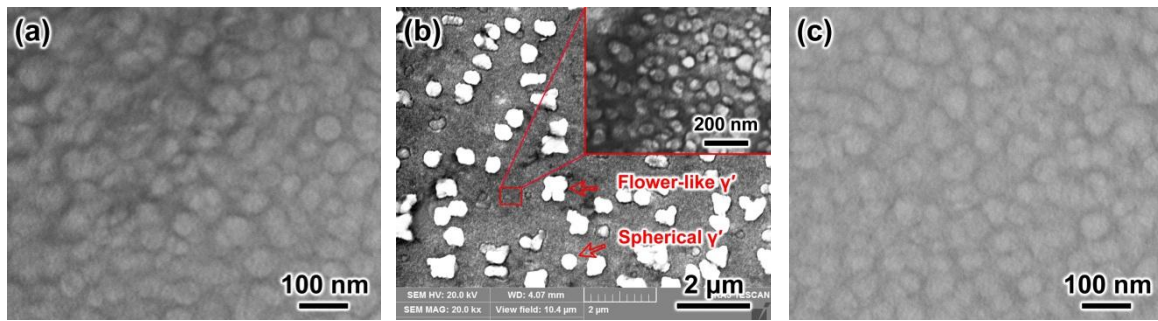
Fig. 4 (a) γ′ phase precipitated during the water quenching process in the samples held for 5 minutes at 1140 °C, (b) undissolved secondary γ′ precipitates and γ′ phase precipitated during the water quenching process after hot deformation at 1110 °C, (c) γ′ phase precipitated during the water quenching process after hot deformation at 1140 °C.

Fig. 5 illustrates the misorientation angle evolution of the samples deformed at different conditions. The correlated misorientation plot shows the misorientation data between neighboring points in a data set and the uncorrelated misorientation plot indicates the misorientation between random points in this set. When the deformation was performed at the temperature of 1110 °C and the strain rate of 0.01 s^{-1}, the misorientation distribution shifted from LAGBs to HAGBs with the increase of strain. The fractions of LAGBs at 0.11, 0.36 and 0.69 were calculated as 50.00%, 27.18% and 5.67%, respectively. Correspondingly, the average misorientation angles at the strains of 0.11, 0.36 and 0.69 were determined as 16.65°, 28.20° and 41.63°, respectively. The decrease of fraction of LAGBs and the increase of the average misorientation angle were both related to the DRX process. As mentioned above, the generation and multiplication of dislocations led to a strong strain hardening at the beginning of deformation, and then LAGBs formed via dislocation rearrangement. However, DRX process was restrained by the deformation stored energy at this stage, large amount of LAGBs hence survived, which was also verified by Fig. 2(b). DRX process became easier with the increase of strain due to the increasing driving force for the movement of

13

dislocations and migration of GBs. Therefore, the fraction of LAGBs fell from 50.00% to 27.18% when the strain increased from 0.11 to 0.36. At the strain of 0.69, deformed grains were almost replaced by the DRX grains, and only few LAGBs existed (5.67%). Meanwhile, with the exception of a strong increase in approximately 60°, the difference between the uncorrelated misorientation plot and the random curve gradually decreased with the increase of strain (Fig. 5(a)–(c)). It indicates that the texture weakened with continuous strain when the deformations were carried out at 1110 °C [51].

The effects of strain on the misorientation angle distribution were not very sensitive to deformation temperature (compared Fig. 5(a)–(c) and Fig. 5(d)–(f)). However, the temperature did affect the misorientation angle distribution at a certain strain via the effects on DRX process. The samples compressed to 0.69 at 1110 and 1140 °C were used to illustrate the influences (Fig. 5(c) and (f)). The LAGBs fraction of the sample deformed at 1140 °C (7.71%) was higher than that of the sample deformed at 1110 °C (5.67%). It was because that some DRX grains were re-deformed during the continuous compression and substructures occurred again. When deformation was performed at a super-solvus temperature, the DRX grains were easier to be deformed again by comparison to the samples deformed at a sub-solvus temperature. Besides, the average misorientation angle of the sample deformed at 1140 °C was determined as 35.21°, which was lower than that of the sample deformed at 1110 °C. Two factors led to this abnormal behavior. Firstly, the re-formed substructures mentioned above increased the fraction of LAGBs and the average misorientation angle decreased correspondingly. This effect was slight in view of the little difference between the fractions of the LAGBs in the two samples. Secondly, a sharp increase at approximately 60° boundaries could be observed in the correlated misorientation plot of the sample deformed at 1110 °C, which affected the average value of misorientation angle.

The large increase might be attributed to the formation of annealing twins during hot deformation [21].

Fig. 6 shows the distribution of Σ3 twin boundaries of the samples deformed to the strain of 0.69 at 1110 and 1140 °C. It was clear that the fraction of twin boundaries within the sample deformed at 1110 °C was much higher than that of the sample deformed at 1140 °C, which resulted from the effects of γ′ phase. When the deformation was carried out at a sub-solvus temperature (1110 °C in this case), the undissolved γ′ precipitates slowed down grain boundary migration by Smith-Zener pinning, as shown in Fig. 7(a). However, the GBs could be unpinned from the γ′ particles when the driving force was enough, as shown in Fig. 7(b). At this transient, the local velocity of the grain boundary migration could be very fast. Previous investigations indicated the number of Σ3 twins is proportional to the distance over which grain boundaries have moved, and to the velocity of grain boundary migration [41, 52-55]. Fig. 7(c) and (d) indicated the fast migration of GBs resulted in stacking faults in front of the GBs easily, which subsequently developed into the twins [56, 57]. Therefore, the presence of γ′ phase could increase the content of twin boundaries when the deformation was performed at a sub-solvus temperature.
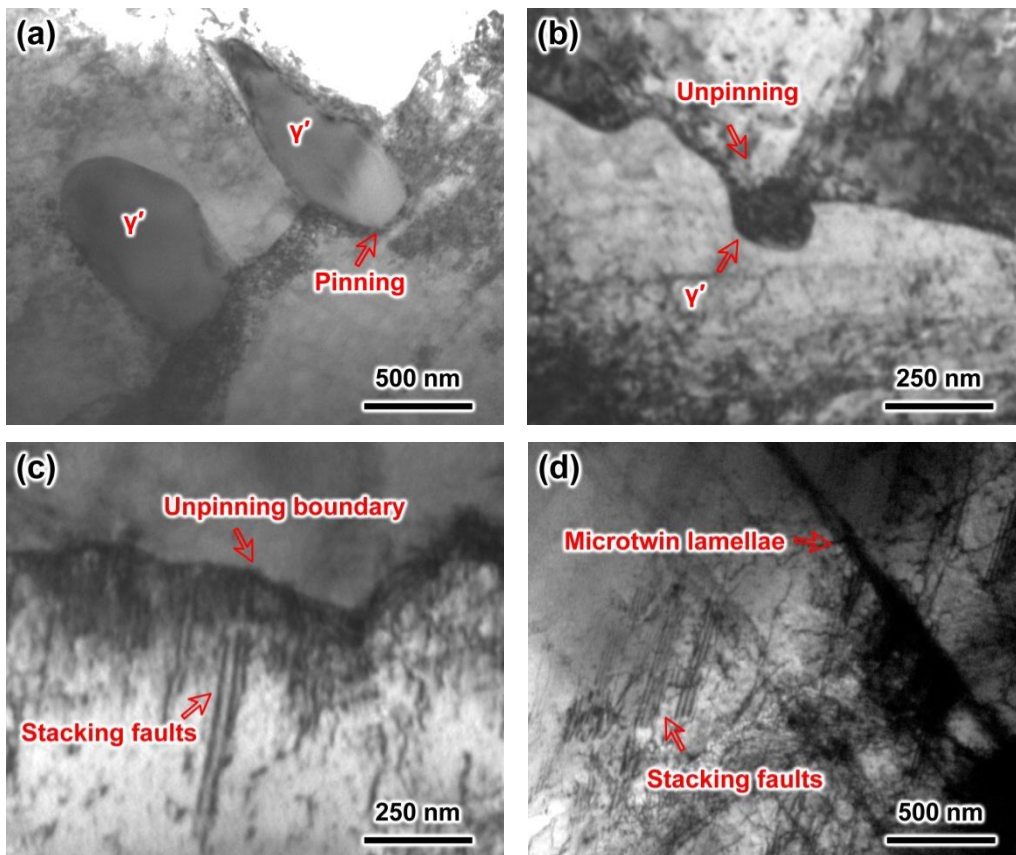
1
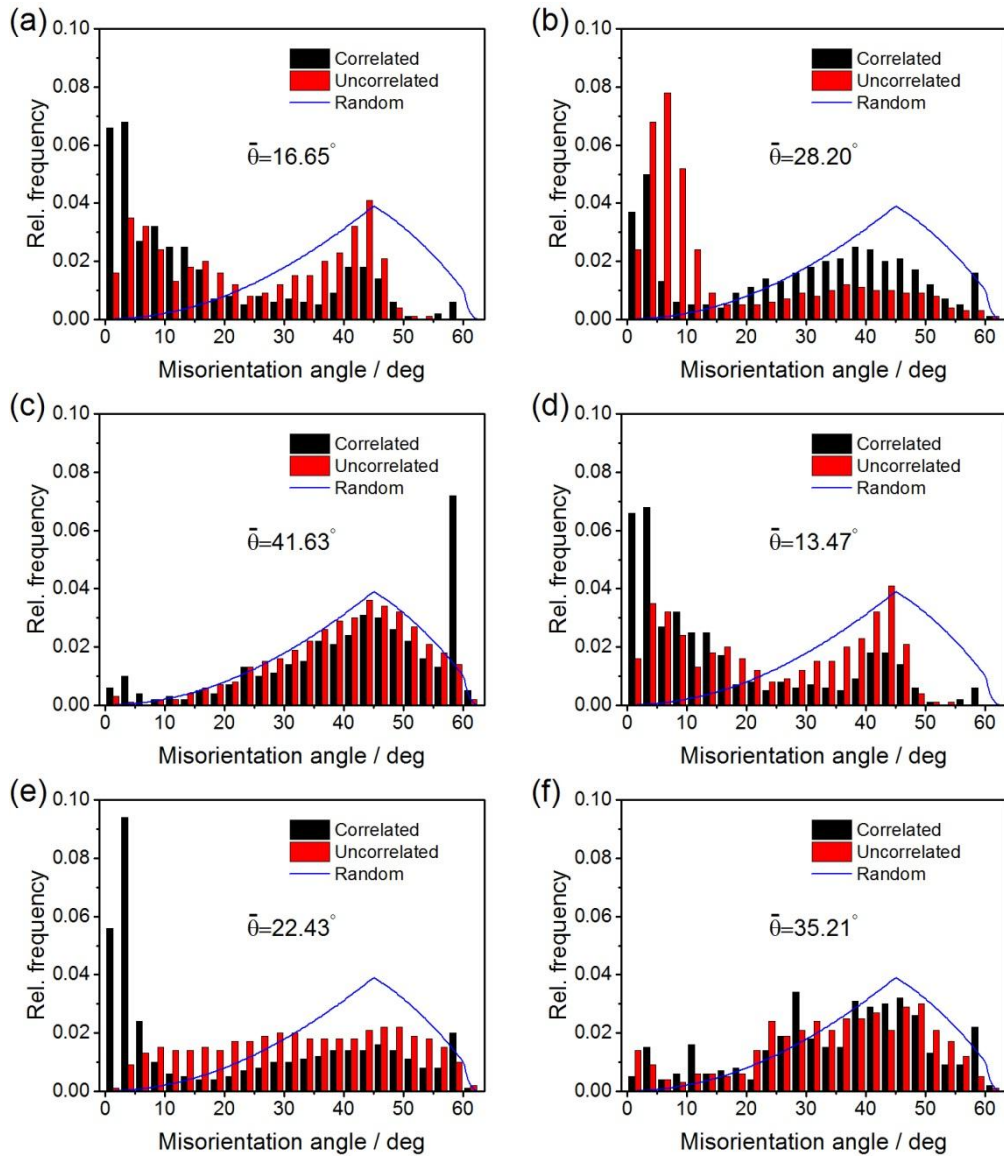
Fig. 5 Misorientation angle distribution of the nickel-based superalloy deformed at different conditions: (a) 1110 °C/ε=0.11, (b) 1110 °C/ε=0.36, (c) 1110 °C/ε=0.69, (d) 1140 °C/ε=0.11, (e) 1140 °C/ε=0.36 and (f) 1140 °C/ε=0.69.
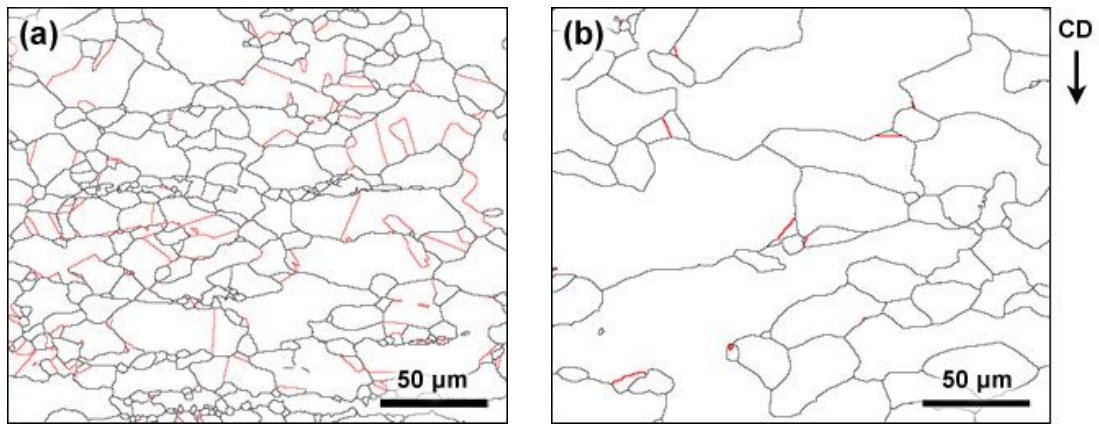
1

2 **Fig. 6** EBSD maps of the samples compressed to the strain of 0.69 at the temperatures of

3 (a) 1110 and (b) 1140 °C. The red lines represent twin boundaries (Σ3 boundaries).

4

5 **Fig. 7** TEM images of the samples deformed at a sub-solvus temperature.

6 *3.2 Microtextural evolution at sub-/super-solvus temperatures*

Fig. 8 demonstrates the microtextural evolution processes of the as-cast superalloy during the sub-solvus and super-solvus deformations by using {100} pole figures. The maximum contour data are also labelled in the individual pole figures. Fig. 8(a) shows that a strong <100> casting texture lay parallel to the direction nearly 45° away from compression direction (CD) towards TD in the initial as-cast samples. When the deformations were performed at a sub-solvus temperature (1110 °C), the texture weakened significantly as the increase of strain. The maximum contour data of textures for the samples compressed to 0.11, 0.36 and 0.69 were 11.60, 4.55 and 2.81, respectively. It indicates that the strain strongly affected the intensities of textures during hot deformation process. Meanwhile, it could be observed that the initial texture decreased in strength and a new <100> ∥ CD textural component appears (Fig. 8(a)–(d)). The new texture was weak and could be attributed to DRX, i.e., the recrystallization texture. [58]. It has been claimed that the recrystallization texture has its origin in either the preferred nucleation of grains with a particular orientations (oriented nucleation theory) or the preferred growth of grains of specific orientations from a more randomly oriented array of nuclei [59]. Texture also weakened with continuous strain when the samples were deformed at 1140 °C (a super-solvus temperature), which was similar with that at 1110 °C. However, two differences should be noted here. Firstly, the initial texture weakened more obviously at the early stage of deformation than that at 1110 °C. The higher deformation temperature benefited the development of DRX, and thus weakened the preexisted texture at that stage. Secondly, by comparison Fig. 8(d) and Fig. 8(g), the sample deformed at a super-solvus temperature exhibited a much stronger texture than that deformed at a sub-solvus temperature. Stronger texture meant more grains with close crystallographic orientations. The higher temperature and the absence of γ′ particles both benefited to the migration of GBs and thus promoted the growth and merging of new DRX grains. DRX grains with close crystallographic orientations converged, while those with random

1 orientation competed with each other and finally the winner devoured the others to generate a

2 bigger grain. This strengthened the texture to some extent and decreased the fraction of

3 HAGBs [60], which was also consistent with the discussion of misorientation distribution in

4 section 3.1. In addition, the size of DRX nuclei, the position of DRX grains and the

5 orientation relationships may all result in grains of some orientations growing faster or slower

6 than others, and thereby influence the recrystallization texture [61]. These will be particularly

7 important in the samples deformed at a super-solvus temperature, 1140 °C in this case. Based

8 on the discussion above, it was more efficient to weaken the initial texture of as-cast

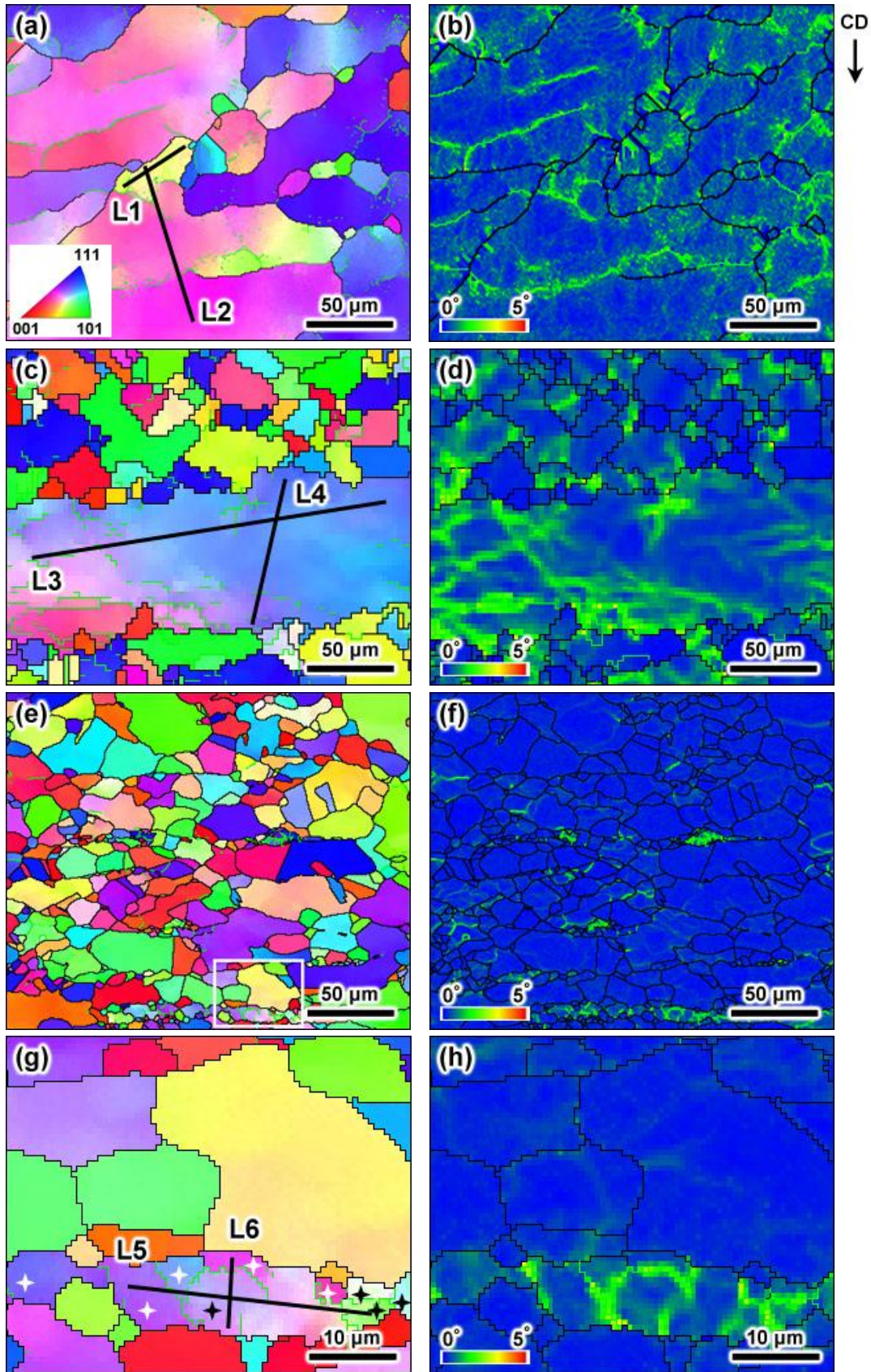9 superalloy at a sub-solvus deformation.
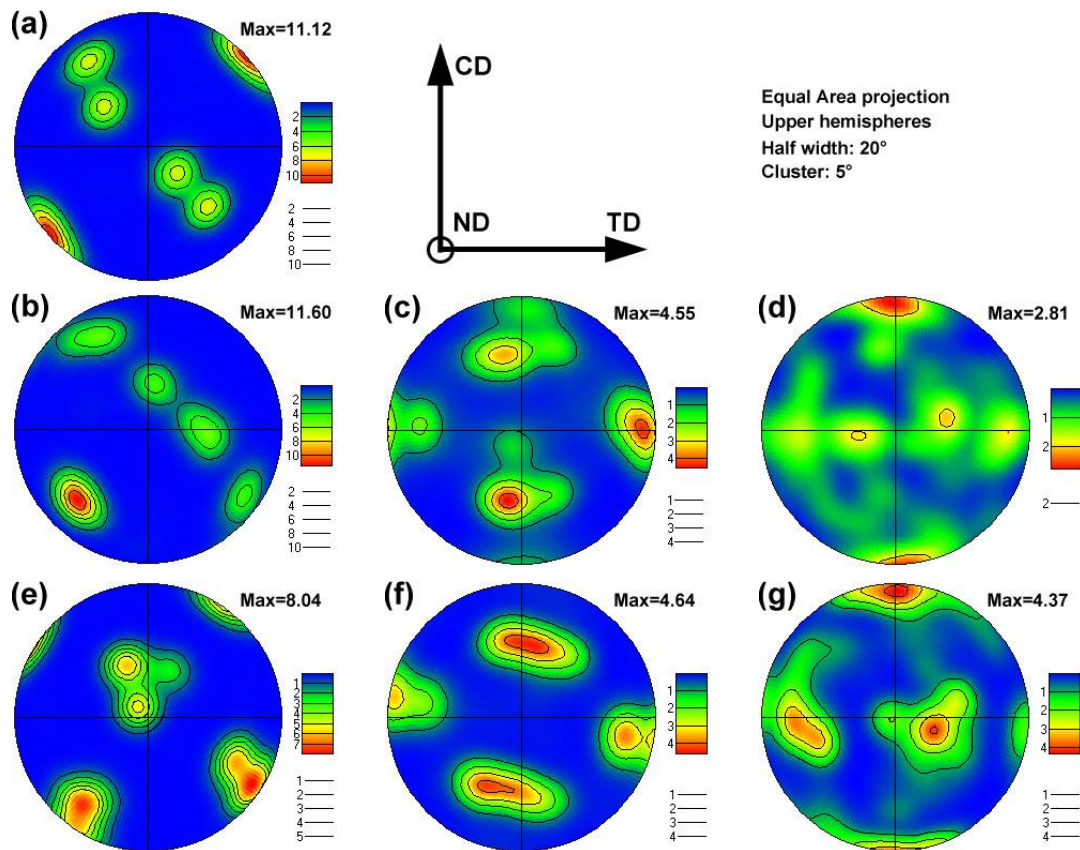
10

11 **Fig. 8** {100} pole figures of (a) the as-cast superalloy and the samples deformed at

12 different conditions: (b) 1110 °C/ε=0.11, (c) 1110 °C/ε=0.36, (d) 1110 °C/ε=0.69, (e)

13 1140 °C/ε=0.11, (f) 1140 °C/ε=0.36 and (g) 1140 °C/ε=0.69.

3.3 Mechanisms of DRX

3.3.1 DDRX at sub-/super-solvus temperatures

Since dynamic recovery is slow for low stacking-fault-energy materials, the microstructural evolution during hot deformation in nickel-based superalloys is mainly associated with DRX [31]. It means that the microstructural evolution is controlled by a nucleation-and-growth process in such cases. Fig. 9 shows the OIM maps and corresponding KAM maps of the samples deformed at 1110 °C. The KAM maps were calculated using nearest neighbor points (a 3×3 region), and the threshold was set to of 5° to avoid grain boundaries contributing to the maps. The DRX grains with lower KAM values (0–1°) could be distinguished from the deformed grains since the local plastic strain or dislocation density in deformed grains were characterized using KAM maps [41, 62]. As shown in Fig. 9(a) and (b), serrated GBs could be observed easily, but few dislocation-free grains were observed nearby the initial GBs. It was recognized that the serrated GBs led to strain induced grain boundary migration (SIBM) and hence provided potential nucleation sites for subsequent DDRX [63-66]. The original deformed grains and new DRX grains both existed when the sample was compressed to the strain of 0.36, shown in Fig. 9(c) and (d). It could be observed that most of the DRX grains nucleated and then developed along the initial GBs. Meanwhile, the grain boundary bulging was obvious nearby the residual initial GBs where the DRX was under development. As shown in Fig. 9(e) and (f), most of grains were entirely blue identified as DRX grains with lower KAM values (0–1°) when the strain increased to 0.69. It indicates that the DRX process almost completed at this stage. However, most of the GBs were still bulging and were reserved by immediate water quenching. It meant that the DDRX still took place at the sample that deformed to a relative large strain (0.69) when the deformation was

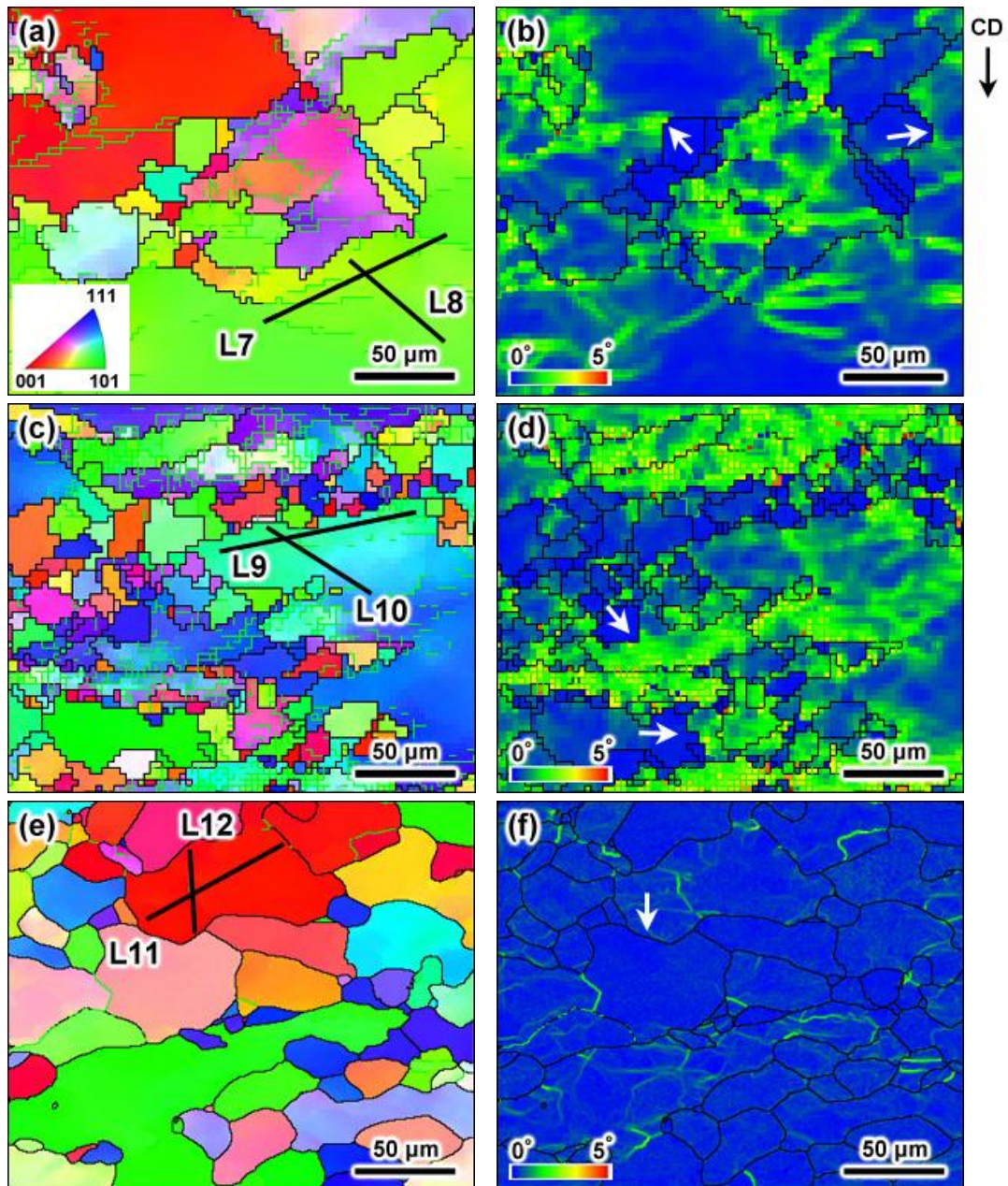1   carried out at sub-solvus temperatures and the strain rate of 0.01 s^{-1}.

Fig. 9 OIM and corresponding KAM maps of the samples deformed to different strains at 1110 °C: (a), (b) ε=0.11, (c), (d) ε=0.36, (e), (f) ε=0.69, (g)(h) the selection marked by a white rectangle in Fig. 9(e).

Fig. 10 exhibits the OIM and corresponding KAM maps of the samples deformed at a super-solvus temperature (1140 °C) and a constant strain rate of 0.01 s^{-1} with different strains. Higher deformation temperature benefited to the arrangement of dislocations and migration of GBs. Meanwhile, the γ′ phase dissolved at a super-solvus temperature, which strongly weakened the resistances of the dislocation movement and grain boundary migration. Both of the two factors could promote the evolution of DRX, especially the growth process of new-fine grains. Several new DRX grains with lower KAM values (0–1°) could be observed nearby the initial GBs when the sample was compressed to the strain of 0.11 at the temperature of 1140 °C and the strain rate of 0.01 s^{-1}, as shown in Fig. 10(a) and (b). DRX became easier here by comparison with that at a sub-solvus temperature. It was found that the GBs between the deformed and DRX grains, marked by arrows in Fig. 10(b), bulged obviously due to the energy difference between the two kinds of grains. It indicates that DDRX took place during the early stage of deformation at a super-solvus temperature. Continuous deformation led to the increase of dislocation density and also the deformation stored energy. Hence, half of the initial deformed grains have been replaced by the new, fine DRX grains in Fig. 10(c) and (d). Almost all DRX grains evolved along the initial GBs and hence generated DRX bands here, which was similar to the behaviors in the samples deformed at 1110 °C. Meanwhile, one could found that the serrated GBs bulged into initial deformed grains (marked by arrows in Fig. 10(d)), and thus were potential sites for subsequent DDRX. Fig. 10(e) and (f) is the OIM and KAM maps of the sample compressed to strain of 0.69 at 1140 °C. DRX was developed at this deformation stage due to sufficient

deformation stored energy, temperature and time. However, the KAM values were higher than 1° within more than half of the grains in Fig. 10(f). It seems to suggest that the DRX degree was lower than that at 1110 °C and the same strain, which was because that the re-deformation of the DRX grains. The higher deformation temperature provided more driving force for the migration of GBs and movement of dislocations. Meanwhile, γ′ phase dissolved when a nickel-base superalloy was deformed at a super-solvus temperature. The peak stress, hence, decreased from 127.67 to 81.83 MPa when deformation temperature increases from 1110 to 1140 °C. It meant that the grains were easier to be re-deformed at 1140 °C. Therefore, it could be concluded that the DRX process completed before the sample was deformed to the strain of 0.69 and the dislocation-free DRX grains were deformed once again during further strain. That was the reason that KAM values were higher than 1° within more than half of the grains in Fig. 10(f). When one focused on the GBs between the grain with the KAM value of ~0° and re-deformed grain, bulging behavior could still be observed due to the dislocation density difference between the two grains (marked by arrows in Fig. 10(f)). Based on discussion above, DDRX occurred during the whole deformation of the samples deformed at super-solvus temperatures. The easier migration of GBs benefited DDRX via grain boundary bulging at higher deformation temperatures.

Fig. 10 OIM and corresponding KAM maps of the samples deformed to different strains at 1140 °C: (a), (b) $\varepsilon=0.11$, (c), (d) $\varepsilon=0.36$, (e), (f) $\varepsilon=0.69$.

3.3.2 CDRX at sub-/super-solvus temperatures

A close examination of Fig.7 and Fig. 10 suggests that the high KAM values distributed near the grain or subgrain boundaries within the deformed grains. It has been recognized that

24

the dislocation density was proportional to the KAM values, i.e. the local misorientation [67-69]. Concentration of high KAM values close to GBs or subgrain boundaries demonstrates an increment of misorientation toward GBs, which indicates the occurrence of dynamic recovery followed by CDRX [70]. CDRX was characterized by progressive lattice rotation and the misorientation profiles across the selected grains were used to confirm the occurrence of CDRX.

As shown in Fig. 11(a), both the cumulative misorientation and local misorientation could not exceed 10° along the initial GBs at a distance about 46 μm. As for the misorientation gradient across the deformed grain, the cumulative misorientation barely exceeded 10° at a distance about 100 μm (Fig. 11(b)). Two abrupt increases could be detected at the positions of 31 and 71 μm on the plot of cumulative misorientation. Meanwhile, two peaks could also be observed at the two positions on the local misorientation plot. Combined with Fig. 9(a), it was found that two subgrain boundaries were located at these two positions. Therefore, the CDRX was under development at a relative low strain (0.11) at a sub-solvus temperature (1110 °C). As the strain increased to 0.36, the cumulative/local misorientation along the initial GBs and across the deformed grains still could not exceed 10° even within a distance of 100 μm, as shown in Fig. 11(c) and (d). However, several misorientation jumps and fluctuation stages meant the formation of different orientation bands, which would be the potential nucleation sites for CDRX by further progressive subgrain rotation [21]. When the strain increased to 0.69, DRX almost completed except few residual deformed grains. Fig. 9(g) and (h) shows the OIM and KAM maps of the selection marked by a white rectangle in Fig. 9(e). It was found that an elongated deformed grain has been divided into at least nine subgrains by several LAGBs. These subgrains were marked by stars, and the white and black colors were just used to provide enough visual contrast to be readable (Fig. 9(g)). The KAM

map (Fig. 9(h)) indicates that this elongated deformed grain had high KAM values distributed near the intragranular LAGBs, which meant large strain and dislocation density gradients within this residual deformed grain. As shown in Fig. 11(e), the cumulative misorientation across this grain rapidly increased to 25° at a distance about 28 μm. Two fluctuation stages on the curve could be clearly observed, which demonstrated two nearly dislocation-free subgrains. Meanwhile, the cumulative misorientation across the deformed grain exceeded 6° at a distance about 4 μm. The misorientation continued to accumulate in subgrains and finally regular grain characters appeared, i.e., a new grain occurred. Therefore, the CDRX characterized by progressive subgrain rotation was developed well when the studied superalloy was compressed to 0.69 at a sub-solvus temperature. It is very different from the DRX mechanisms reported in the fine-grain structures of wrought billets, where DDRX dominates the DRX process and seldom evidence of CDRX can be captured [71].
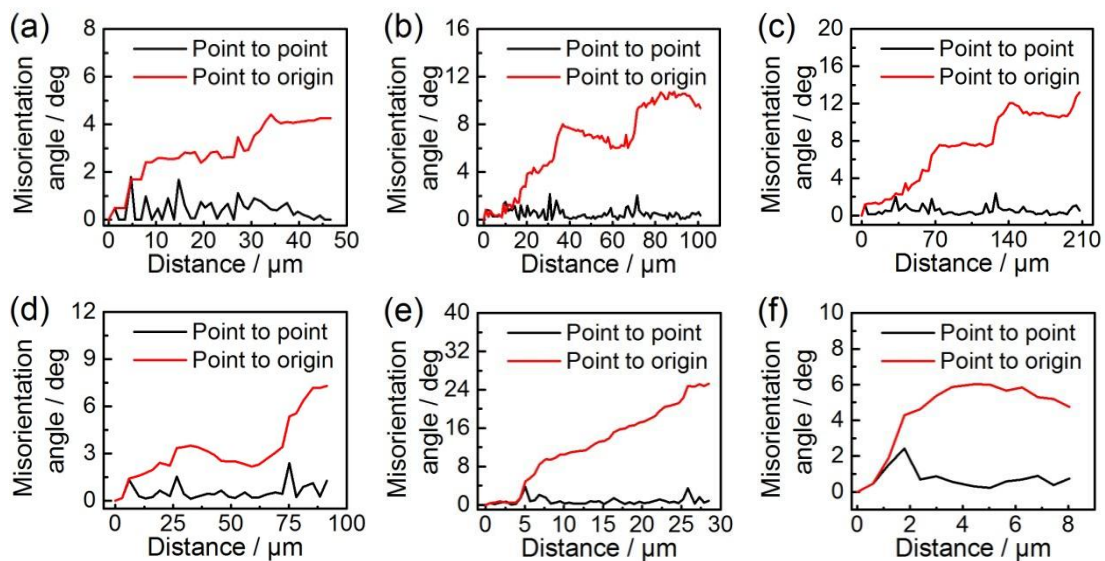
Fig. 11 Misorientation profiles along the lines marked in Fig. 9: (a) L1, (b) L2, (c) L3, (d) L4, (e) L5, (f) L6.

Higher deformation temperature promotes the evolution of DRX and may also influence

its mechanisms [30]. Fig. 12 shows the misorientation profiles along the lines marked in Fig. 10. During the early stage of deformation at a super-solvus temperature (1140 °C), the cumulative misorientation along the initial GBs did not exceed 10° (Fig. 12(a)). However, the local misorientation across this grain did not exceed 2° and the corresponding cumulative misorientation easily reached 9° at a distance of 65 μm (Fig. 12(b)). It means the misorientation gradient within this deformed grain was steady and no obvious orientation bands occurred here. The misorientation gradients along the initial GBs and within the deformed grains increased obviously when the strain increased to 0.36. The local/cumulative misorientations along the initial GBs and across the deformed grains were both beyond 10° at distances of 90 and 56 μm, respectively , as shown in Fig. 12 (c) and (d). It indicates the CDRX nucleation via progressive subgrain rotation was possible here. As for the samples deformed to the strain of 0.69 at 1140 °C, a DRX grain with slight strain caused by re-deformation was selected to plot the misorientation profile. There was no obvious difference between the levels of cumulative misorientation along L11 and L12. Both of them were hard to exceed 4° across the grain, indicating that the misorientation accumulation caused by re-deformation was not enough to give rise to CDRX once again in this re-deformed grain. Therefore, CDRX was under development when the samples were deformed to the strain of 0.69 at a super-solvus temperature, where the first DRX process had finished and the second one were restrained by deformation stored energy. It was reasonable to deduce that the CDRX mechanism would be activated with further increasing strain and DRX would take place once again. CDRX played a less important role during the deformation at a super-solvus temperature by comparison with that at a sub-solvus temperature.
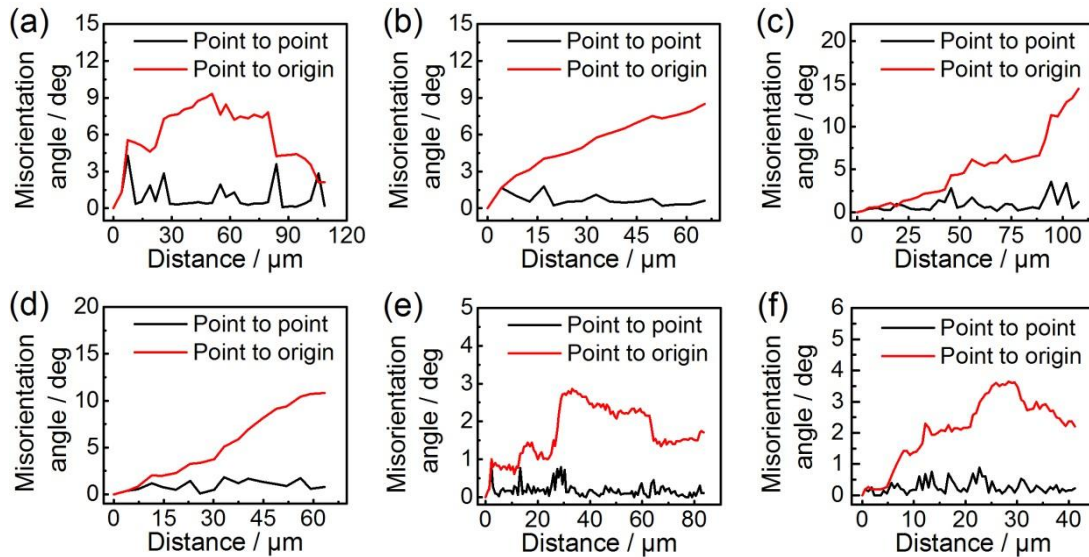
Fig. 12 Misorientation profiles along the lines marked in Fig. 10: (a) L7, (b) L8, (c) L9, (d) L10, (e) L11, (f) L12.

CDRX features the progressive subgrain rotation. Subgrain rotation is an extension of the recovery process [72], which is achieved by the movement and interaction of dislocations to form a subgrain wall [73]. Subsequently, the LAGBs generated via recovery process may transform into HAGBs if there are sufficient deformation stored energy, deformation temperature and time. Hence, the CDRX mechanism often leads to an increased fraction of 10–15° misorientation [21]. Fig. 13 is the fractions of different misorientation angle scopes at different deformation temperatures. The fraction of GBs with 10–15° misorientation obviously increased in the samples deformed at 1110 °C and the strain of 0.11. Meanwhile, similar behavior was also observed in the samples deformed at 1140 °C and the strain of 0.69. Combined with the results from the discussion of OIM and misorientation profiles above, it could be concluded that CDRX did not dominate the DRX process of the studied superalloy although this mechanism was activated at both sub-solvus and super-solvus temperatures.
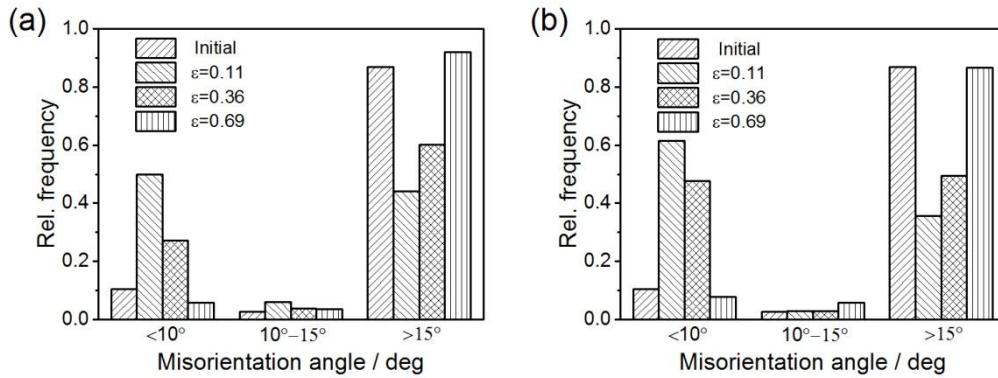
Fig. 13 Fractions of different misorientation angle scopes at (a) 1110 and (b) 1140 °C.

4. Conclusions

In order to improve the understanding of DRX behaviors and mechanisms during the cogging process of nickel-based ingots, an as-cast superalloy was hot compressed by a Gleeble-3500 simulator. Special attention was focused on the microstructural evolution associated DRX at both sub-solvus and super-solvus temperatures. Several concluding remarks from this research were summarized in the following:

(1) Increasing strain led to the increase in the volume fraction of DRX grains at both sub-solvus and super-solvus temperatures, and also the fraction of HAGBs. As strain increased, both the correlated and uncorrelated misorientations approached the random distribution.

(2) The absence of γ' phase and the more driving force from higher temperatures promoted the migration of GBs, which resulted in the coarsening of DRX grains during deformation at super-solvus temperatures.

(3) At super-solvus temperatures, DRX grains with close crystallographic orientations converged much more easily, while those with random orientation competed with each other and finally the winner devoured the others to generate a bigger grain. This strengthened the texture to some extent, and hence it was more efficient to weaken the initial textures of an as-cast superalloy at a sub-solvus deformation.

(4) DDRX dominated the DRX process during the deformation of the studied superalloy at both sub-solvus and super-solvus temperatures. CDRX was the second mechanism and played a very important role during the deformation at a sub-solvus temperature due to the limited ability of grain boundary migration. It is different from the DRX mechanisms reported in the fine-grain structures of wrought billets, where DDRX dominates the DRX process and seldom evidence of CDRX can be captured.

Acknowledgements

Data availability

The raw/processed data required to reproduce these findings cannot be shared at this time as the data also forms part of an ongoing study.

References

[1] F.J. Humphreys, M. Hatherly, Chapter 13–Hot deformation and dynamic restoration, in:

1   F.J. Humphreys, M. Hatherly (Eds.), Recrystallization and Related Annealing

2   Phenomena (Second Edition), Elsevier, Oxford, 2004, pp. 427–428.

3   [2] D.X. Wen, Y.C. Lin, J. Chen, X.M. Chen, J.L. Zhang, Y.J. Liang, L.T. Li, Work-hardening

4   behaviors of typical solution-treated and aged Ni-based superalloys during hot

5   deformation, J. Alloys Compd. 618 (2015) 372–379.

6   [3] B.C. Xie, B.Y. Zhang, Y.Q. Ning, M.W. Fu, Mechanisms of DRX nucleation with grain

7   boundary bulging and subgrain rotation during the hot working of nickel-based

8   superalloys with columnar grains, J. Alloys Compd. 786 (2019) 636–647.

9   [4] S.V. Mehtonen, L.P. Karjalainen, D.A. Porter, Hot deformation behavior and

10   microstructure evolution of a stabilized high-Cr ferritic stainless steel, Mater. Sci. Eng. A

11   571 (2013) 1–12.

12   [5] M.E. Kassner, S.R. Barrabes, New developments in geometric dynamic recrystallization,

13   Mater. Sci. Eng. A 410-411 (2005) 152–155.

14   [6] Y. Wu, H. Kou, Z. Wu, B. Tang, J. Li, Dynamic recrystallization and texture evolution of

15   Ti–22Al–25Nb alloy during plane-strain compression, J. Alloys Compd. 749 (2018)

16   844–852.

17   [7] F.J. Humphreys, M. Hatherly, Chapter 14–Continuous recrystallization during and after

18   large strain deformation, in: F.J. Humphreys, M. Hatherly (Eds.), Recrystallization and

19   Related Annealing Phenomena (Second Edition), Elsevier, Oxford, 2004, pp. 451–467.

20   [8] X.L. An, B. Zhang, C.L. Chu, L. Zhou, P.K. Chu, Evolution of microstructures and

21   properties of the GH4169 superalloy during short-term and high-temperature processing,

22   Mater. Sci. Eng. A 744 (2019) 255–266.

23   [9] M.Q. Ou, Y.C. Ma, H.L. Ge, W.W. Xing, Y.T. Zhou, S.J. Zheng, K. Liu, Microstructure

24   evolution and mechanical properties of a new cast Ni-base superalloy with various Ti

25   contents, J. Alloys Compd. 735 (2018) 193–201.

[10] D.X. Wen, Y.C. Lin, X.H. Li, S.K. Singh, Hot deformation characteristics and dislocation substructure evolution of a nickel-base alloy considering effects of δ phase, J. Alloys Compd. 764 (2018) 1008–1020.

[11] S.S.S. Kumar, T. Raghu, P.P. Bhattacharjee, G.A. Rao, U. Borah, Work hardening characteristics and microstructural evolution during hot deformation of a nickel superalloy at moderate strain rates, J. Alloys Compd. 709 (2017) 394–409.

[12] C. Zhang, L.W. Zhang, W.F. Shen, Q.H. Xu, Y. Cui, The processing map and microstructure evolution of Ni-Cr-Mo-based C276 superalloy during hot compression, J. Alloys Compd. 728 (2017) 1269–1278.

[13] J.Y. Chen, J.X. Dong, M.C. Zhang, Z.H. Yao, Deformation mechanisms in a fine-grained Udimet 720LI nickel-base superalloy with high volume fractions of gamma' phases, Mater. Sci. Eng. A 673 (2016) 122–134.

[14] V. Anil Kumar, R.K. Gupta, S.V.S. Narayana Murty, A.D. Prasad, Hot workability and microstructure control in Co20Cr15W10Ni cobalt-based superalloy, J. Alloys Compd. 676 (2016) 527–541.

[15] J. Kwong, D.A. Axinte, P.J. Withers, The sensitivity of Ni-based superalloy to hole making operations: Influence of process parameters on subsurface damage and residual stress, J. Mater. Process. Tech. 209 (2009) 3968–3977.

[16] X.Y. Qin, D.W. Huang, X.J. Yan, X.Y. Zhang, M.J. Qi, S. Yue, Hot deformation behaviors and optimization of processing parameters for Alloy 602 CA, J. Alloys Compd. 770 (2019) 507–516.

[17] Z.P. Wan, T. Wang, Y. Sun, L.X. Hu, Z. Li, P.H. Li, Y. Zhang, Dynamic softening mechanisms of GH4720Li alloy during hot deformation, Acta Metall. Sin. 55 (2019) 213–222.

[18] S.S.S. Kumar, T. Raghu, P.P. Bhattacharjee, G. Appa Rao, U. Borah, Evolution of

microstructure and microtexture during hot deformation in an advanced P/M nickel base superalloy, Mater. Charact. 146 (2018) 217–236.

[19] K.A. Babu, Y.H. Mozumder, R. Saha, V.S. Sarma, S. Mandal, Hot-workability of super-304H exhibiting continuous to discontinuous dynamic recrystallization transition, Mater. Sci. Eng. A 734 (2018) 269–280.

[20] G. He, L. Tan, F. Liu, L. Huang, Z. Huang, L. Jiang, Unraveling the formation mechanism of abnormally large grains in an advanced polycrystalline nickel base superalloy, J. Alloys Compd. 718 (2017) 405–413.

[21] Y.C. Lin, X.Y. Wu, X.M. Chen, J. Chen, D.X. Wen, J.L. Zhang, L.T. Li, EBSD study of a hot deformed nickel-based superalloy, J. Alloys Compd. 640 (2015) 101–113.

[22] Y.Q. Ning, Z.K. Yao, M.W. Fu, H.Z. Guo, Recrystallization of the hot isostatic pressed nickel-base superalloy FGH4096: I. Microstructure and mechanism, Mater. Sci. Eng. A 528 (2011) 8065–8070.

[23] S. Mitsche, C. Sommitsch, D. Huber, M. Stockinger, P. Poelt, Assessment of dynamic softening mechanisms in Allvac® 718Plus™ by EBSD analysis, Mater. Sci. Eng. A 528 (2011) 3754–3760.

[24] C. Rehrl, S. Kleber, O. Renk, R. Pippan, Effect of grain size in compression deformation on the microstructural evolution of an austenitic stainless steel, Mater. Sci. Eng. A 540 (2012) 55–62.

[25] A. Belyakov, K. Tsuzaki, H. Miura, T. Sakai, Effect of initial microstructures on grain refinement in a stainless steel by large strain deformation, Acta Mater. 51 (2003) 847–861.

[26] A.I. Fernández, P. Uranga, B. López, J.M. Rodriguez-Ibabe, Dynamic recrystallization behavior covering a wide austenite grain size range in Nb and Nb-Ti microalloyed steels, Mater. Sci. Eng. A 361 (2003) 367–376.

[27] M. El Wahabi, L. Gavard, F. Montheillet, J.M. Cabrera, J.M. Prado, Effect of initial grain size on dynamic recrystallization in high purity austenitic stainless steels, Acta Mater. 53 (2005) 4605–4612.

[28] F.L. Li, R. Fu, F.J. Yin, D. Feng, H.Z. Wang, G. Du, Y. Feng, Impact of γ'(Ni$_3$(Al,Ti)) phase on dynamic recrystallization of a Ni-based disk superalloy during isothermal compression, J. Alloys Compd. 693 (2017) 1076–1082.

[29] H. Zhang, K. Zhang, Z. Lu, C. Zhao, X. Yang, Hot deformation behavior and processing map of a γ'-hardened nickel-based superalloy, Mater. Sci. Eng. A 604 (2014) 1–8.

[30] H. Zhang, K. Zhang, S. Jiang, H. Zhou, C. Zhao, X. Yang, Dynamic recrystallization behavior of a γ'-hardened nickel-based superalloy during hot deformation, J. Alloys Compd. 623 (2015) 374–385.

[31] S.L. Semiatin, D.S. Weaver, R.C. Kramb, P.N. Fagin, M.G. Glavicic, R.L. Goetz, N.D. Frey, M.M. Antony, Deformation and recrystallization behavior during hot working of a coarse-grain, nickel-base superalloy ingot material, Metall. Mater. Trans. A 35 (2004) 679–693.

[32] M.G. Glavicic, P.A. Kobryn, F. Spadafora, S.L. Semiatin, Texture evolution in vacuum arc remelted ingots of Ti-6Al-4V, Mater. Sci. Eng. A 346 (2003) 8–18.

[33] F.F. Liu, J.Y. Chen, J.X. Dong, M.C. Zhang, Z.H. Yao, The hot deformation behaviors of coarse, fine and mixed grain for Udimet 720Li superalloy, Mater. Sci. Eng. A 651 (2016) 102–115.

[34] J. Chen, J. Dong, M. Zhang, Z. Yao, Deformation mechanisms in a fine-grained Udimet 720LI nickel-base superalloy with high volume fractions of γ' phases, Mater. Sci. Eng. A 673 (2016) 122–134.

[35] Z. Wan, L. Hu, Y. Sun, T. Wang, Z. Li, Microstructure evolution and dynamic softening mechanisms during high-temperature deformation of a precipitate hardening Ni-based

superalloy, Vacuum 155 (2018) 585–593.

[36] Y. Chen, R. Prasath babu, T.J.A. Slater, M. Bai, R. Mitchell, O. Ciuca, M. Preuss, S.J. Haigh, An investigation of diffusion-mediated cyclic coarsening and reversal coarsening in an advanced Ni-based superalloy, Acta Mater. 110 (2016) 295–305.

[37] L. Tan, Y. Li, F. Liu, Y. Nie, L. Jiang, Microstructure evolutions of a powder metallurgy superalloy during high-strain-rate deformation, J. Alloys Compd. 789 (2019) 506–517.

[38] Z.L. Zhao, Y.Q. Ning, H.Z. Guo, Z.K. Yao, M.W. Fu, Discontinuous yielding in Ni-base superalloys during high-speed deformation, Mater. Sci. Eng. A 620 (2015) 383–389.

[39] S.L. Semiatin, J.M. Shank, A.R. Shiveley, W.M. Saurber, E.F. Gaussa, A.L. Pilchak, The efect of forging variables on the supersolvus heat-treatment response of powder-metallurgy nickel-base superalloys, Metall. Mater. Trans. A 45 (2014) 6231–6251.

[40] C. Aoki, T. Ueno, T. Ohno, K. Oikawa, Influence of hot-working conditions on grain growth of superalloy 718, J. Mater. Process. Tech. 267 (2019) 26–33.

[41] D. Jia, W. Sun, D. Xu, L. Yu, X. Xin, W. Zhang, F. Qi, Abnormal dynamic recrystallization behavior of a nickel based superalloy during hot deformation, J. Alloys Compd. 787 (2019) 196–205.

[42] Y. Liu, Y. Wu, J. Yu, J. Ju, Z. Zhang, M. Kang, J. Wang, B. Sun, Y. Ning, Temperature-dependent deformation mechanisms and microstructural degradation of a polycrystalline nickel-based superalloy, J. Alloys Compd. 775 (2019) 181–192.

[43] Y. Zhao, S. Fu, S. Zhang, X. Tang, N. Liu, G. Zhang, An aAdvanced cast/wrought technology for GH720Li alloy disk from fine grain ingot, in: E.A. Ott, J.R. Groh, A. Banik, I. Dempster, T.P. Gabb, R. Helmink, X. Liu, A. Mitchell, G.P. Sjöberg, A. Wusatowska-Sarnek (Eds.) Superalloy 718 and Derivatives, 2012, pp. 271–280.

[44] S. Vernier, J.-M. Franchet, C. Dumont, N. Bozzolo, A mechanism leading to gamma'

precipitates with {111} facets and unusual orientation relationships to the matrix in gamma-gamma' nickel-based superalloys, Metall. Mater. Trans. A 49A (2018) 4308–4323.

[45] A. Seret, C. Moussa, M. Bernacki, N. Bozzolo, On the coupling between recrystallization and precipitation following hot deformation in a γ-γ′ nickel-based superalloy, Metall. Mater. Trans. A 49 (2018) 4199–4213.

[46] Q.Y. Yu, Z.H. Yao, J.X. Dong, Deformation and recrystallization behavior of a coarse-grain, nickel-base superalloy Udimet720Li ingot material, Mater. Charact. 107 (2015) 398–410.

[47] S.B. Lee, D.Y. Yoon, M.F. Henry, Abnormal grain growth and grain boundary faceting in a model Ni-base superalloy, Acta Mater. 48 (2000) 3071–3080.

[48] S.B. Lee, D.Y. Yoon, N.M. Hwang, M.F. Henry, Grain boundary faceting and abnormal grain growth in nickel, Metall. Mater. Trans. A 31 (2000) 985–994.

[49] H. Gleiter, Theory of grain boundary migration rate, Acta Mater. 17 (1969) 853–862.

[50] H. Gleiter, The mechanism of grain boundary migration, Acta Mater. 17 (1969) 565–573.

[51] Z. Liu, P. Li, L. Xiong, T. Liu, L. He, High-temperature tensile deformation behavior and microstructure evolution of Ti55 titanium alloy, Mater. Sci. Eng. A 680 (2017) 259–269.

[52] N. Bozzolo, N. Souaï, R.E. Logé, Evolution of microstructure and twin density during thermomechanical processing in a γ-γ′ nickel-based superalloy, Acta Mater. 60 (2012) 5056–5066.

[53] C.S. Pande, M.A. Imam, B.B. Rath, Study of annealing twins in FCC metals and alloys, Metall. Trans. A 21 (1990) 2891–2896.

[54] W. Wang, F. Brisset, A.L. Helbert, D. Solas, I. Drouelle, M.H. Mathon, T. Baudin, Influence of stored energy on twin formation during primary recrystallization, Mater. Sci. Eng. A 589 (2014) 112–118.

[55] T.S. Prithiv, P. Bhuyan, S.K. Pradhan, V. Subramanya Sarma, S. Mandal, A critical evaluation on efficacy of recrystallization vs. strain induced boundary migration in achieving grain boundary engineered microstructure in a Ni-base superalloy, Acta Mater. 146 (2018) 187–201.

[56] L. Bracke, L. Kestens, J. Penning, Direct observation of the twinning mechanism in an austenitic Fe–Mn–C steel, Scripta Mater. 61 (2009) 220–222.

[57] B.Q. Li, B. Li, Y.B. Wang, M.L. Sui, E. Ma, Twinning mechanism via synchronized activation of partial dislocations in face-centered-cubic materials, Scripta Mater. 64 (2011) 852–855.

[58] F.J. Humphreys, M. Hatherly, Chapter 12–Recrystallization Textures, in: F.J. Humphreys, M. Hatherly (Eds.), Recrystallization and Related Annealing Phenomena (Second Edition), Elsevier, Oxford, 2004, pp. 379–413.

[59] F.J. Humphreys, M. Hatherly, Chapter 12–Recrystallization Textures, in: F.J. Humphreys, M. Hatherly (Eds.), Recrystallization and Related Annealing Phenomena (Second Edition), Elsevier, Oxford, 2004, p. 393.

[60] U.F.H.R. Suhuddin, S. Mironov, Y.S. Sato, H. Kokawa, C.W. Lee, Grain structure evolution during friction-stir welding of AZ31 magnesium alloy, Acta Mater. 57 (2009) 5406–5418.

[61] F.J. Humphreys, M. Hatherly, Chapter 12–Recrystallization Textures, in: F.J. Humphreys, M. Hatherly (Eds.), Recrystallization and Related Annealing Phenomena (Second Edition), Elsevier, Oxford, 2004, pp. 395–396.

[62] Y. Cao, H.S. Di, Research on the hot deformation behavior of a Fe-Ni-Cr alloy (800H) at temperatures above 1000 °C, J. Nucl. Mater. 465 (2015) 104–115.

[63] T. Sakai, Dynamic recrystallization microstructures under hot working conditions, J. Mater. Process. Tech. 53 (1995) 349–361.

[64] H.J. McQueen, C.A.C. Imbert, Dynamic recrystallization: plasticity enhancing structural development, J. Alloys Compd. 378 (2004) 35–43.

[65] P. Poelt, C. Sommitsch, S. Mitsche, M. Walter, Dynamic recrystallization of Ni-base alloys—Experimental results and comparisons with simulations, Mater. Sci. Eng. A 420 (2006) 306–314.

[66] I. Shimizu, Theories and applicability of grain size piezometers: The role of dynamic recrystallization mechanisms, J. Struct. Geol. 30 (2008) 899–917.

[67] Q. Zeng, B. Luan, Y. Wang, X. Zhang, R. Liu, K.L. Murty, Q. Liu, Effect of initial orientation on dynamic recrystallization of a zirconium alloy during hot deformation, Mater. Charact. 145 (2018) 444–453.

[68] C. Moussa, M. Bernacki, R. Besnard, N. Bozzolo, About quantitative EBSD analysis of deformation and recovery substructures in pure Tantalum, IOP Conf. Series: Mater. Sci. Eng. 89 (2015) 12–38.

[69] Y.A. Betanda, A.L. Helbert, F. Brisset, M.H. Mathon, T. Waeckerle, T. Baudin, Measurement of stored energy in Fe-48%Ni alloys strongly cold-rolled using three approaches: Neutron diffraction, Dillamore and KAM approaches, Mater. Sci. Eng. A 614 (2014) 193–198.

[70] J. Zhao, J. Zhong, F. Yan, F. Chai, M. Dargusch, Deformation behaviour and mechanisms during hot compression at supertransus temperatures in Ti-10V-2Fe-3Al, J. Alloys Compd. 710 (2017) 616–627.

[71] J. Qu, X. Xie, Z. Bi, J. Du, M. Zhang, Hot deformation characteristics and dynamic recrystallization mechanism of GH4730 Ni-based superalloy, J. Alloys Compd. 785 (2019) 918–924.

[72] A. Halfpenny, D.J. Prior, J. Wheeler, Analysis of dynamic recrystallization and nucleation in a quartzite mylonite, Tectonophysics 427 (2006) 3–14.

[73] S. White, Effects of strain on microstructures, fabrics, and deformation mechanisms in quartzites, Philos. T. R. Soc. A 283 (1976) 69–86.